TU Delft

Delft University of Technology

Chitosan Oligosaccharide Laser Lithograph

A Facile Route to Porous Graphene Electrodes for Flexible On-Chip Microsupercapacitors

Huang, Qian Ming; Yang, Huiru; Wang, Shaogang; Liu, Xu; Tan, Chunjian; Zong, Qihang; French, Paddy; Zhang, Guoqi; Ye, Huaiyu; More Authors

DOI
10.1021/acsami.4c02139

Publication date
2024

Document Version
Final published version

Published in
ACS Applied Materials and Interfaces

Citation (APA)
Huang, Q. M., Yang, H., Wang, S., Liu, X., Tan, C., Zong, Q., French, P., Zhang, G., Ye, H., & More Authors (2024). Chitosan Oligosaccharide Laser Lithograph: A Facile Route to Porous Graphene Electrodes for Flexible On-Chip Microsupercapacitors. *ACS Applied Materials and Interfaces*, *16*(27), 35651-35665. https://doi.org/10.1021/acsami.4c02139

Important note
To cite this publication, please use the final published version (if applicable).
Please check the document version above.

Copyright
Other than for strictly personal use, it is not permitted to download, forward or distribute the text or part of it, without the consent of the author(s) and/or copyright holder(s), unless the work is under an open content license such as Creative Commons.

Takedown policy
Please contact us and provide details if you believe this document breaches copyrights.
We will remove access to the work immediately and investigate your claim.

This work is downloaded from Delft University of Technology.
For technical reasons the number of authors shown on this cover page is limited to a maximum of 10.

Green Open Access added to TU Delft Institutional Repository

'You share, we take care!' - Taverne project

https://www.openaccess.nl/en/you-share-we-take-care

Otherwise as indicated in the copyright section: the publisher is the copyright holder of this work and the author uses the Dutch legislation to make this work public.

ACS APPLIED MATERIALS & INTERFACES

www.acsami.org

Research Article

Chitosan Oligosaccharide Laser Lithograph: A Facile Route to Porous Graphene Electrodes for Flexible On-Chip Microsupercapacitors

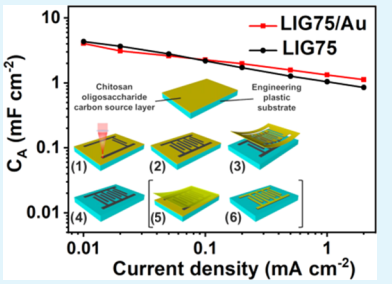
Qian-Ming Huang, Huiru Yang, Shaogang Wang, Xu Liu, Chunjian Tan, Qihang Zong, Chenshan Gao, Shizhen Li, Paddy French, Guoqi Zhang, and Huaiyu Ye*

Cite This: *ACS Appl. Mater. Interfaces* 2024, 16, 35651−35665

Read Online

ACCESS | Metrics & More | Article Recommendations | Supporting Information

ABSTRACT: In this study, a convenient chitosan oligosaccharide laser lithograph (COSLL) technology was developed to fabricate laser-induced graphene (LIG) electrodes and flexible on-chip microsupercapacitors (MSCs). With a simple one-step CO_2 laser, the pyrolysis of a chitosan oligosaccharide (COS) and in situ welding of the generated LIGs to engineering plastic substrates are achieved simultaneously. The resulting LIG products display a hierarchical porous architecture, excellent electrical conductivity (6.3 Ω sq^{-1}), and superhydrophilic properties, making them ideal electrode materials for MSCs. The pyrolysis−welding coupled mechanism is deeply discussed through cross-sectional analyses and finite element simulations. The MSCs prepared by COSLL exhibit considerable areal capacitance of over 4 mF cm^{-2}, which is comparable to that of the polyimide-LIG-based counterpart. COSLL is also compatible with complementary metal−oxide−semiconductor (CMOS) and micro-electro-mechanical system (MEMS) processes, enabling the fabrication of LIG/Au MSCs with comparable areal capacitance and lower internal resistance. Furthermore, the as-prepared MSCs demonstrate excellent mechanical robustness, long-cycle capability, and ease of series-parallel integration, benefiting their practical application in various scenarios. With the use of eco-friendly biomass carbon source and convenient process flowchart, the COSLL emerges as an attractive method for the fabrication of flexible LIG on-chip MSCs and various other advanced LIG devices.



KEYWORDS: *laser-induced graphene, microsupercapacitor, flexible on-chip electronics, chitosan oligosaccharide, laser lithograph*

Downloaded via TU DELFT on July 22, 2024 at 12:56:55 (UTC).
See https://pubs.acs.org/sharingguidelines for options on how to legitimately share published articles.

INTRODUCTION

With the advent of the Internet of Things (IoT) era, the demand for efficient and integrable miniature energy storage devices has surged, driven by the widespread use of wireless sensor net nodes, portable electronics, etc.[1−5] This has underscored the necessity for reliable power sources that can ensure a stable and long-term energy supply.[5−7] Micro-supercapacitors (MSCs) play a pivotal role in miniature energy systems, proving particularly well-suited for IoT nodes requiring frequent charging and discharging.[8,9] Their distinct advantages, including high power density, overlong cycle capability, and superior reliability compared to conventional battery units, make them indispensable.[10−12] In the realm of flexible electronics, to facilitate the development of flexible System-on-Chip units with integrated energy harvesting, storage, and application modules, considerable efforts have been invested in constructing customized on-chip all-solid-state MSCs with interdigital electrode structures on diverse engineering polymer substrates.[13−18]

Over the past few decades, various patterning technologies have been extensively explored for crafting conductive interdigital architectures and flexible in-plane MSCs. These methods encompass photolithography, inkjet/screen/three-dimensional (3D) printing, and more.[19−22] However, achieving a satisfactory balance among crucial metrics such as precision, eco-friendliness, and cost has proven challenging with these approaches. Recently, Tour's group introduced a compelling direct laser writing (DLW) method that stands out as a competitive option.[23] This innovative technique allows for the one-step direct printing of 3D porous graphene electrodes on polymer substrates, enabling the fabrication of all-solid-state flexible MSCs.[24−27] The one-step DLW method boasts several advantages, including noncontact mask-free processing, convenient pattern design, high resolution, and low energy consumption.[28,29] The resulting 3D hierarchical laser-induced graphene (LIG) exhibits excellent electrical conductivity, a large specific surface area, and high mechanical strength, making it an ideal electrode material for MSC construction.[30−32] Since its introduction, this approach has paved the

Received: February 6, 2024
Revised: May 11, 2024
Accepted: June 11, 2024
Published: June 26, 2024



ACS Publications

© 2024 American Chemical Society

way for the development of numerous MSCs, including electrical double-layer, pseudo-, and hybrid capacitors based on LIGs.[33−36]

The role of polymer precursor substrates is crucial in both the formation of LIG and the preparation of reliable MSC devices, serving as both the carbon matrix and mechanical support.[26,37] Among these substrates, plastic polymer films stand out as the foremost and most commonly utilized precursors for LIG isolation.[38−40] Their attributes, including lightweight, excellent insulation, and high thermal and mechanical robustness, ensure the dependable use of prepared flexible devices.[41−44] Unfortunately, not all engineering plastics can be directly converted into the desired LIGs, limiting the practical applications of LIG devices in various scenarios. This constraint underscores the persistent need for innovative carbon feedstocks in LIG electronics. Recent studies have revealed that natural renewable materials, along with their individual-component extracts or processed goods, can serve as carbon precursors for producing high-quality LIGs and advancing micronano devices, especially those rich in lignin or cellulose structures.[38,45−47] These new materials boast broad sources, environmental friendliness, and high biocompatibility, offering a viable path toward green and sustainable LIG electronics.[48,49] Despite the advantages, these materials often fall short as flexible supporting films due to their intrinsically poor mechanical and physicochemical characteristics and face limitations in preparing highly reliable and antiaging LIG devices.[50,51] For instance, extensively studied paper-based LIG devices are extremely vulnerable to high-temperature combustion, water infiltration, mechanical tearing, etc.[52−54] While methods like common reverse-mold peeling have been developed to transfer LIG to robust substrates for enhanced reliability,[25,55] the transfer process often damages the architectures of LIGs, significantly impacting the final device performance. Consequently, exploring innovative green precursors while ensuring the preparation of highly reliable devices proves to be a formidable challenge for LIG electronics, particularly for flexible on-chip MSCs featuring meticulously designed in-plane electrodes.

Chitosan, a renewable biopolymer derived from chitin—a primary component of marine crustacean shells and one of the most abundant natural polymers on Earth—stands out for its vast availability.[56,57] Beyond the broad sources, chitosan-based materials also exhibit compelling characteristics, including biocompatibility, biodegradability, and nontoxicity.[58,59] In addition, their highly soluble property enables easy preparation into polymer films, positioning them as promising new-type carbon sources for LIG electronic fabrication. Recent endeavors have showcased the conversion of component-stable chitosan-based composites or derivatives into conductive LIGs,[60−62] and these developments have extended to the creation of electrochemical sensors[60,61] and triboelectric nanogenerators.[62] However, in contrast to lignocellulosic counterparts, reliability issues are more pronounced with chitosan-based substrates hosting conformal LIG electrodes. These thin films are notably susceptible to brittleness or deformation under slight variations in temperature, humidity, or mechanical stress. Such reliability challenges pose a significant obstacle, particularly for on-chip MSCs with an intricate interdigital electrode architecture. The use of water-containing gel electrolytes exacerbates the problem, and can easily lead to deformation of the hydrophilic substrate and consequent device failure. Therefore, to the best of our knowledge, no chitosan-based polymer-derived LIG MSCs have been reported to date due to this formidable reliability challenge. In this study, we introduce a pioneering chitosan oligosaccharide laser lithography (COSLL) technology for LIG synthesis and reliable MSC preparation. In this process, chitosan oligosaccharide (COS) is blade-coated onto the heterogeneous engineering plastic films, forming conformal double-layer structures. Subsequently, employing a simple one-step CO_2 laser treatment, the COS carbon source layer undergoes facile pyrolysis to yield meticulously crafted LIG interdigital electrodes, and the resulting film electrodes are securely bonded to the engineering polymer substrate. After a further peeling-off process to remove the residual precursor, LIG electrodes can be packaged into desired on-chip MSCs, and the devices exhibit both high reliability and high performance. Herein, we report the COSLL method, the physical and chemical natures of COS-derived LIG, and the electrochemical performance of the corresponding flexible LIG on-chip MSCs.

EXPERIMENTAL SECTION

Preparation of LIG Electrodes and MSCs. The chosen biomass precursor for this study is a highly soluble chitosan oligosaccharide (Figure S2, M_W < 3000), purchased from Shanghai Yuanye Bio-Technology Co., Ltd. A COS and poly(vinyl alcohol) (PVA) mixture with a ratio of 3:2 was sequentially added to a beaker containing deionized water with a ratio of 20. This mixture was continuously stirred on a hot stage at 100 °C for about 1 h, resulting in a fully dissolved dark brown COS/PVA solution. The COS/PVA solution, with the desired viscosity, was then applied to the surface of plastic films using a simple blade-coating process. All used substrate films, including polycarbonate (PC), poly(methyl methacrylate) (PMMA), and poly(ethylene terephthalate) (PET), were purchased from Taobao stores and their thickness is about 270 μm. After approximately 4 h of thermal evaporation at ambient conditions, a dry COS/PVA composite film adhered closely to the substrate film was obtained with a thinness of about 80 μm. Here, PVA served as a binder in the film preparation and was fully decomposed during laser treatment.[63] Laser-engraving was carried out using a commercial 10.6 μm CO_2 laser system (Jilin Yongli Laser Technology Co., Ltd.) under ambient conditions (temperature ∼ 25 °C, humidity ∼ 50%). The specific processing parameters are detailed in Figure S1. To ensure high-quality LIG products, a defocused process was adopted, allowing convenient adjustment of the output laser power by setting the duty cycle. The duty cycle was employed to represent the laser power, ensuring realistic and accurate experimental records, and LIG prepared at a duty cycle of X% is denoted as LIG10X. Additional metal Au deposition was achieved using commercial magnetron sputtering equipment (KTZ1650PVD, Zhengzhou Ketan Instrument Equipment Co., Ltd.) and the deposition rate of the Au source is about 8.3 Å s^{-1}.

The preparation of MSC was based on the COS/PVA carbonaceous source layer and PC support layer. LIG interdigital electrodes were prepared using one-step CO_2 laser processing, and the residual COS/PVA was removed by a straightforward mechanical exfoliation. For efficient removal, a water-assisted peel-off process was utilized. The highly soluble COS enabled the laser-treated sample to be immersed in cold deionized water for 3−5 s, enhancing the plasticity and toughness of the residual COS/PVA for smooth peeling. After peeling-off, the wet LIG electrodes on the PC film were dried using a constant-temperature oven. For the preparation of LIG/Au interdigital electrodes, 3 min of Au deposition was performed to load Au to the surface of LIG electrodes before the peeling-off process. The packaging structure of LIG MSCs is detailed in Figure S13. The conductive LIG paths on both sides of the interdigital electrodes were bonded with a copper tape through silver pastes for electrical connection to the external circuit. Dragon skin was

https://doi.org/10.1021/acsami.4c02139
ACS Appl. Mater. Interfaces 2024, 16, 35651−35665

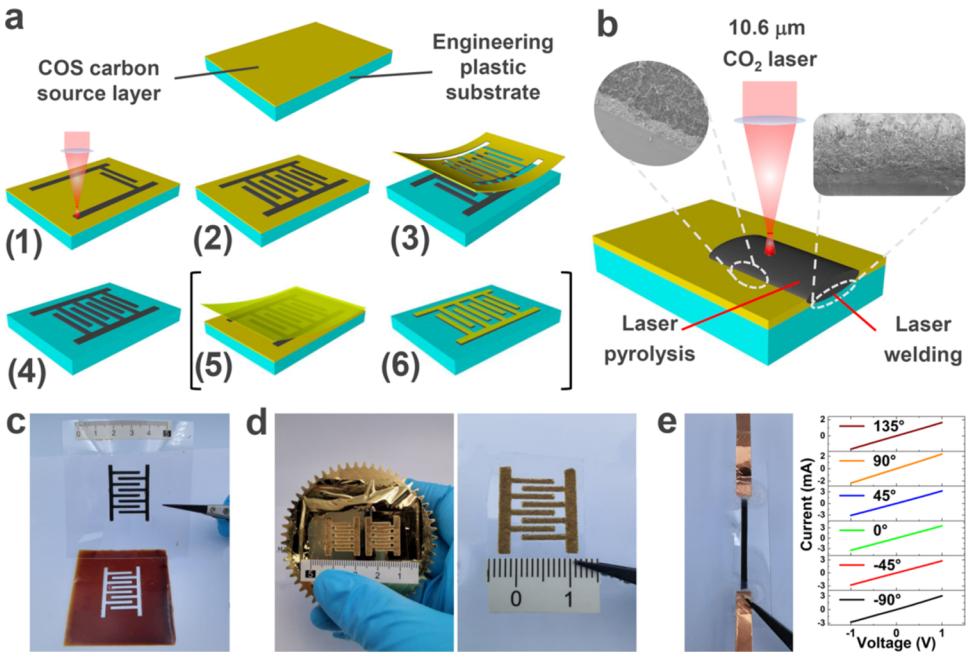


Figure 1. Schematic diagrams of COSLL technology and target LIG patterns on engineering plastic substrates. (a) Flowchart illustrating the COSLL process, mainly including blade-coating, laser-engraving, and peeling-off (steps 5−6): additional metal target deposition before removal. (b) Model depicting the simultaneous laser pyrolysis graphitization of the COS/PVA precursor and laser welding of resulting LIG to functional plastic substrate. (c) Laser-printed LIG interdigital electrodes on a PC substrate alongside mechanically stripped COS/PVA residue films. (d) Au-deposited LIG/Au composite interdigital electrodes on the PC film. (e) Conformal LIG resistor (30 × 2 mm^2) on the PC film and its I−V characteristic curves at different degrees of bending.

employed as an encapsulation material for surrounding insulation. By dropping a prefabricated H_2SO_4/PVA gel electrolyte (1.0 mol L^{-1}) onto the central active interdigital electrodes, target in-plane MSCs can be obtained. It is important to note that, to obtain an all-solid flexible LIG MSC for electrochemical testing, the prepared devices need to be placed in a fume hood for about 24 h to allow the electrolyte to completely solidify.

General Characterization Studies. Optical images with relatively low magnifications were captured using a mobile phone camera or a normal photomicroscope. The surface and cross-sectional morphology of as-fabricated LIGs were examined by secondary-electron scanning electron microscopy (SEM, Regulus SU8230) at an accelerating voltage of 5 kV, with samples gold-sprayed before imaging to enhance surface conductivity. The average value of the cross-sectional LIG is considered as its reference thickness. Transmission electron microscopy (TEM) and high-resolution TEM measurements were performed using a FEI-TALOS-F200X device. For TEM imaging, LIG powder was scratched from the surface of the plastic substrate, dispersed into an absolute alcohol solution, and then dripped onto a 200-mesh copper grid with a supporting carbon membrane for observation. X-ray diffraction (XRD) analyses were conducted on a Bruker D8 Advance diffractometer equipped with graphite monochromator Cu Kα radiation (λ = 1.54186 Å) in the 2θ range of 10−80°, with a scanning step width of 0.02°. Raman spectra were recorded via a Laser Confocal Raman Spectrometer (LabRAM HR Evolution) with a 532 nm incident laser at room temperature. Both sheet resistance (R_S) and two-wire resistance were measured using a Keithley 6510 equipped with alligator clips and a four-point probe. Surface chemical analysis of both COS/PVA and LIGs was obtained using the X-ray photoelectron spectroscopy (XPS) apparatus (PHI 5000 Versaprobe III, ULVAC-PHI) with an Al Kα X-ray source and a base pressure of 10^{-7} Torr. The fine C spectra were recorded in 0.125 eV step size with a pass energy of 69 eV, corrected using the contaminated C 1s peak (284.8 eV) as the reference. The contact angles of water droplets on target surfaces were measured with a contact angle meter (Dongguan Shengding Precision Instrument Co., Ltd.). Thermogravimetric analysis (TGA) was performed on a Mettler TGA2 thermal analyzer. Powder LIG samples were placed in an Al_2O_3 crucible, with an empty crucible used as a reference, and heated from 30 to 1000 °C at a rate of 10 °C min^{-1} under a nitrogen atmosphere. It is worth noting that for all cyclic bending durability tests, the bending state is achieved through an integrated linear motor (Jinan Mengchuang Technology Co., Ltd.) equipped with two supporting fixtures.

Electrochemical Measurement and Calculation. Cyclic voltammetry (CV), galvanostatic charge−discharge (GCD), and electrochemical impedance spectroscopy (EIS) tests were conducted on a CHI800D electrochemical workstation (Shanghai Chenhua Instrument Co., Ltd.). All measurements were conducted in ambient conditions. The electrochemical impedance spectra of MSCs were measured at open circuit voltage with a sinusoidal voltage amplitude of 20 mV in the frequency range from 1 MHz to 0.01 Hz. Specific areal capacitance (C_A) of the MSC devices was calculated from CV and GCD measurements according to eqs 1 and 2

$$C_{A/CV} = \frac{\int I(V)\mathrm{d}V}{2Av\Delta V} \tag{1}$$

where $\int I(V)\mathrm{d}V$ is the integrated area from the CV curve; $I(V)$ is the current response for voltage scan; A is the total active electrode area (0.48 cm^{-2} in the study); ν is the voltage scan rate; and ΔV is the voltage window

$$C_{A/GCD} = \frac{I\Delta t}{A\Delta V} \tag{2}$$

where I is the applied discharge current and Δt is the discharge time.

The areal energy density (E_A) and power density (P_A) of the MSCs were calculated from $C_{A/GCD}$ by eqs 3 and 4, respectively

$$E_A = \frac{1}{2}\frac{C_{A/GCD}\Delta V^2}{3600} \tag{3}$$

$$P_A = \frac{3600E_A}{\Delta t} \tag{4}$$

https://doi.org/10.1021/acsami.4c02139
ACS Appl. Mater. Interfaces 2024, 16, 35651−35665

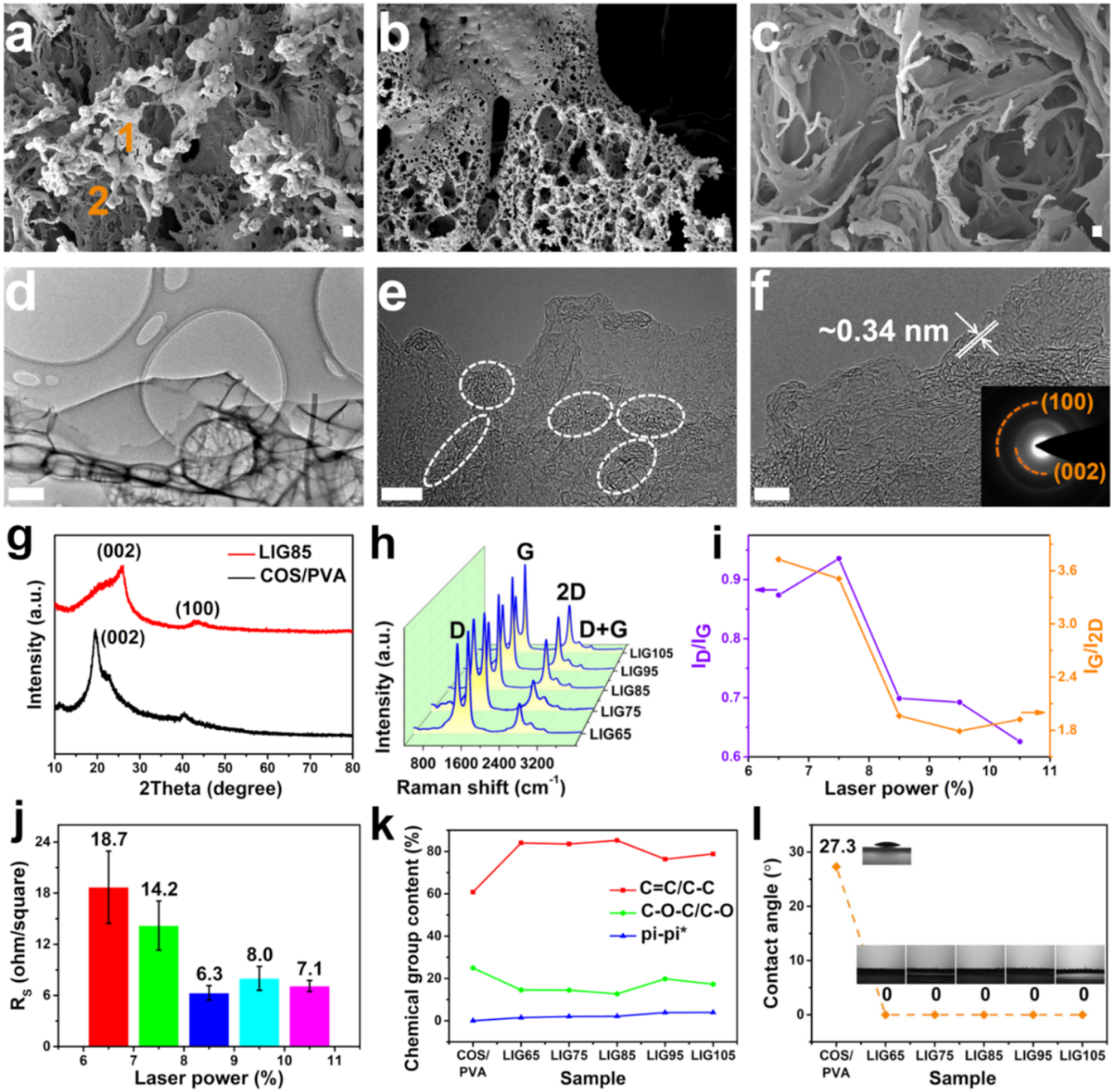


Figure 2. Microscopic morphologies and physicochemical properties of the as-prepared LIG products derived from COS. (a) SEM image of LIG obtained at a laser power of 8.5% (LIG85), featuring a scale bar of 10 μm. (b, c) High-resolution SEM images captured from site 1 and site 2 of panel (a), showcasing scale bars of 1 μm. (d) TEM image of LIG85, accompanied by a scale bar of 1 μm. (e, f) High-resolution TEM images of LIG85, highlighting scale bars of 10 and 5 nm, respectively. Oval marks in panel (e) draw attention to the clustered nanopores, while the inset in panel (f) reveals the SAED pattern. (g) XRD patterns of LIG85 and COS/PVA. (h) Raman spectra of LIGs fabricated at different laser powers. (i) Correlation between the calculated I_D/I_G and I_G/I_{2D} ratios and laser power. (j) Sheet resistance (R_S) of LIGs obtained at various laser powers. (k) Chemical group composition determined from the fitting of C 1s spectra of COS/PVA and different LIG samples. (l) Contact angles formed by water on the surfaces of COS/PVA and various LIG samples.

where 3600 is a conversion factor from Ws to Wh.

RESULTS AND DISCUSSION

The comprehensive process flow diagram for the COSLL method is depicted in Figure 1a. Initially, a uniformly mixed solution of COS and PVA was meticulously blade-coated onto the surface of the plastic substrate. This process resulted in the formation of a snug-fitting bilayer film structure through conformal contact. Given the remarkably high water solubility of COS, PVA was selected as the binder to achieve effective blade-coating without interfering in the subsequent LIG formation.[63] Subsequently, the conformal composite film underwent exposure to a 10.6 μm CO_2 infrared laser. The COS/PVA layer was instantaneously pyrolyzed into LIG electrodes, precisely following the predesigned interdigital shapes (Figure 1a, steps 1−2). The unexposed and dry-transferable residual COS/PVA was then efficiently removed through a straightforward or water-assisted mechanical peeling-

https://doi.org/10.1021/acsami.4c02139
ACS Appl. Mater. Interfaces 2024, 16, 35651−35665

off process, leaving only the bare LIG electrodes adhered to the plastic substrate (Figure 1a, steps 3−4). It is worth noting that the water-assisted peeling-off is more efficient and lossless, especially for high-precision patterning with smaller critical dimensions but requires an additional postdrying treatment. Moreover, COSLL seamlessly integrates with the film deposition process of the complementary metal−oxide semiconductor (CMOS) or micro-electro-mechanical system (MEMS) processes (Figure 1a, steps 5−6). With the metal deposition before the removal step, the metal target will be deposited onto the surface of the interdigital structure and COS/PVA serves as a barrier layer at this point. Figure 1b provides a more detailed model of COSLL, proposing that the technique can be dissected into two independent parts: laser pyrolysis and laser welding. The upper COS carbon source layer undergoes successful conversion into the target LIG material through intense laser pyrolysis, and the generated LIGs are then closely fused to the surface of the substrate film through a laser thermal fusion connection. A more in-depth discussion of the pyrolysis−welding coupled mechanism will be provided later.

The COSLL method was applied to pattern LIG electrodes on various engineering plastic films. In Figure S3a, an optical photograph showcases the as-prepared COS/PVA film attached to the surface of a PC substrate. As depicted in Figure 1c, through a single CO_2 laser-engraving step, dark brown COS/PVA can be easily transformed into black LIGs, and after the removal process, interdigital LIG electrodes on the PC film are obtained, with unexposed residues stripped off without causing damage. Thanks to the convenience afforded by COSLL, interdigitated LIG electrodes can be easily prepared in batches (Figure S3b), laying the foundation for the modular integration of MSC devices. The developed process also allows for the realization of arbitrary LIG patterns on the PC substrate (Figure S3c), which provides opportunities for the free design and functionalization of LIG products. In addition, COSLL demonstrates excellent compatibility with other common engineering plastics, such as PMMA and PET (Figure S3d,e). Nevertheless, over a wide process range, the resulting LIG on these substrates appears to have large holes caused by gas release, which affects the conductivity of the electrodes and the performance of the fabricated device more or less. Figure 1d showcases the LIG/Au composite electrode obtained through magnetron sputtering based on gold target, which is beneficial for enhancing the electrical conductivity of the LIG network. Furthermore, a LIG resistor was prepared, and its linear voltammetry curves were tested at different bending degrees (Figure 1e). The results illustrate that its resistances remain stable at random angles, underscoring the remarkable conformal electrical properties of LIG for flexible applications.

The COSLL method stands out for its ability to transform arbitrarily designed graphics into tangible conductive LIG products on diverse substrates. This capability aligns with the standard definition of a lithography process. When compared to traditional lithography (Figure S4), COSLL boasts the advantage of not necessitating additional masks, development steps, or metal layer depositions. This streamlined approach enhances the convenience of preparing flexible on-chip devices, including MSCs. Notably, as previously mentioned, COS can also serve as a dry-transferable photoresist, facilitating additional CMOS or MEMS-based metal film deposition processes. This application can be harnessed to craft LIG−metal composite electrodes and MSCs with superior performance. While DLW represents the simplest among the three technologies (Figure S4), it cannot directly fabricate reliable devices based on carbon source substrates with weak mechanical properties, such as chitosan-based materials. In contrast, COSLL excels by enabling in situ transfer of the generated LIG to a heterogeneous target substrate through the establishment of a double-layer structure comprising a carbon source layer and a support layer. This unique feature contributes to the creation of highly reliable devices from chitosan-based precursors. In essence, the eco-friendliness inherent in the core COS carbon precursor, combined with the simplicity of the processing steps, renders COSLL an exceedingly attractive technology for the fabrication of LIG MSCs and other advanced devices.

The microscopic morphology and physicochemical characteristics of COS-derived LIGs were subject to thorough investigation. SEM images of LIG85 reveal the presence of distinctive coral-like hierarchical porous structures (Figure 2a), resembling those observed in pure COS-derived LIGs.[62] Further insights from high-resolution SEM photos (Figure 2b,2c) expose the intricate composition of the coral-like miniature body, comprised of lamellar thin layers and profoundly stereoscopic macropore architectures. Close to the substrate's inner surface, a discernible fiber structure becomes apparent. The dense bubble macropores likely result from the release of gaseous products (CO, H_2O, CO_2, etc.) during the drastic decomposition of precursors,[23] while the fibrous structure may emerge from the mixing of cooled LIGs and the molten pool of the substratum. It is worth noting that a previous study indicated that the decomposition of the binder PVA does not yield carbon materials;[63] however, the gaseous products may still play an important role in fostering the creation of porous configurations. TEM images further unveil the thin-layer structure and nanopore distributions of LIG85. As depicted in Figure 2d, the randomly stacked sheet carbon structures exhibit evident megapores (>200 nm) and macropores (>50 nm) with smooth edges, and possible white speckled pore structures can be seen in high-resolution TEM (Figure 2e), which are similar to the TEM images of lignin-LIG.[63] These interleaved carbon structures and the randomly distributed nanopore networks of varying sizes reflect the intricate reaction kinetics during laser pyrolysis. The intricate porous architectures of LIGs imply a wealth of electrochemically active sites, providing ample channels for electrolyte diffusion and ion transport. This intricacy significantly contributes to the enhanced electrochemical performance of MSCs.

The evolution of multihole morphology driven by variations in laser power was meticulously examined through SEM and TEM characterizations. The samples denoted as LIG65−LIG105, are obtained at different laser powers ranging from 6.5 to 10.5%. Despite the increase in laser power, the unique coral-like structures of LIGs display minimal changes in SEM images (Figure S5). High-resolution SEM photos consistently reveal prominent porous, lamellar, and fibrous subunits across all cases. Notably, at higher powers (8.5−10.5%), the vertical growth of fiber structures in the bottom region gradually diminished, leaving behind only transversely distributed root-like networks. This shift may be attributed to more intense decomposition under higher temperature and pressure environments. Further microscopic changes in morphology with varying laser power were characterized through TEM

https://doi.org/10.1021/acsami.4c02139
ACS Appl. Mater. Interfaces 2024, 16, 35651−35665

imaging (Figure S6). Low-magnification TEM images indicated that all cases exhibited analogous randomly stacked configurations of macroporous structures. High-resolution TEM images unveiled dense porous units on the surface of the carbon sheets. Notably, the contrast change suggested that the LIGs exhibited a more favorable few-layer property as the laser power increased from 6.5 to 8.5%. A more detailed high-resolution TEM image of LIG85 (Figure 2f) revealed clear strip bands, with each strip representing a single-layer graphene. This phenomenon is often induced by thermal stress, leading to edge bending after laser pyrolysis.[23] A characteristic *d*-space of ∼3.4 Å, measured from adjacent fringes, aligned with the interplanar spacing of the neighboring (002) crystalline planes of graphitic carbons. The selected area electron diffraction (SAED) pattern (inset of Figure 2f) presented two evident rings indexed to (002) and (001) peaks, indicating the presence of polycrystalline structures and demonstrating the graphitic lattice of LIG85. In summary, these analyses of morphological evolution underscore that the desired 3D hierarchical porous LIG materials can be successfully obtained on PC substrates using the COSLL technique within a specific power range.

The graphitic carbon architecture of LIGs was further substantiated through XRD measurements (Figure 2g). LIG85 exhibits a distinctly different distribution of diffraction peaks compared to its precursor COS/PVA. The dominant peak centered at 2θ = 26.1° is attributed to the diffraction of the (002) crystal plane of graphitic carbon.[23] The asymmetric ridge type of (002) suggests the presence of lattice distortion and defects in the as-prepared LIG, as reflected in the emergence of the (100) secondary peak. This diffraction pattern aligns well with the SAED pattern in Figure 2f. In contrast, for COS/PVA, the intense peak centered at 2θ = 19.6° is attributed to the (002) crystal face of PVA, as COS is generally less crystalline. The Raman spectra reveal characteristic peaks (D, G, and 2D) of graphitic carbon in the as-fabricated LIG samples (Figure 2h), which are distinctly different from its precursor COS/PVA (Figure S7). The G peaks at 1570−1581 cm^{-1}, representing the in-plane vibration of sp^2-bonded carbon atoms in the hexagonal graphene lattice, are the most prominent. The D peaks at 1338−1343 cm^{-1} are associated with defects and disorders in LIGs, while the 2D peaks at 2672−2680 cm^{-1}, originating from second-order Raman scattering, are related to the symmetry of the graphene lattice.[64] At a low laser power of 3%, only wide D and G peaks can be measured, and COS begins to transform into amorphous carbon (Figure S8a,b). With an increased laser power of 6%, an additional 2D peak becomes observable due to the formation of low-graphitic carbon. However, if a high power of 12% is applied, the laser radiation induces significant thermal damage to the matrix. As the laser power increases from 6.5 to 10.5%, the I_D/I_G and I_G/I_{2D} ratios exhibit an overall downward trend, with a clear step observed between 7.5 and 8.5% (Figure 2i). This step indicates relatively high laser power can lead to lower defects and better few-layer characteristics of LIGs. These Raman analyses suggest that higher laser power levels generally promote the formation of high-quality LIG materials, provided they avoid causing thermal damage. Conversely, LIG electrodes obtained at lower laser powers, such as LIG75, may harbor abundant defective or distorted sites, potentially enhancing the capacitance of MSCs.

Electrical conductivity serves as another pivotal parameter for evaluating the quality of LIG material. The sheet resistance of LIGs exhibits an initial decrease followed by a slight increase as the laser power is elevated, ultimately reaching a remarkable minimum of 6.3 Ω sq^{-1} at a laser power level of 8.5% (Figure 2j). This ultralow sheet resistance is on par with certain common values found in plastic polymers (15 Ω sq^{-1} for PI-LIG)[23] or lignocellulosic materials-derived LIGs (10 Ω sq^{-1} for wood-LIG).[45] However, when the samples are produced using a laser power of 3%, the average sheet resistance experiences a dramatic surge, exceeding 2 kΩ sq^{-1} due to a lower degree of graphenization (Figure S8c). Conversely, using excessively high power levels (12%) renders it challenging to obtain stable measurements due to damage to the LIG structures. Consequently, our study establishes that a laser power range spanning from 6.5 to 10.5% is deemed ideal for the synthesis of high-quality LIGs for the fabrication of high-performance MSCs. In addition, LIG85 with the lowest sheet resistance is a possible excellent candidate for the preparation of MSCs featuring low internal resistance.

Chemical component analyses were carried out using surface XPS characterization. As depicted in Figure S9, dominant carbon (C) and some oxygen (O) elements were detected in LIGs, and their C/O ratios significantly increased to a range of 6.4−8.1 in comparison to the COS/PVA precursor with a C/O ratio of 2.3 (Table S2). This notable increase could be attributed to the laser-induced carbonization process. The O impurities should exist in defect sites or superficial active groups and are introduced during laser processing in the atmospheric air. Notably, no nitrogen element was detected in the generated LIGs when compared to the COS/PVA matrix. This absence of N can be attributed to the volatilization of nitrogen in gaseous form during intense laser pyrolysis. The deconvolution of the C 1s spectra further allowed for the determination of various chemical groups in both COS/PVA and LIGs (Figure S10). The C 1s spectrum of COS/PVA reveals the presence of unique C−N and N═C−O units due to the existence of N; in contrast, LIGs predominantly contain C═C/C−O, C−O−C/C−O, and $\pi-\pi^*$ bonds. As illustrated in Figure 2k, with an increase in laser power, the concentration of C═C/C−C bonds in LIGs significantly increases compared to the precursor, peaking at a laser power of 8.5%. Conversely, the content of C−O−C/C−O bonds decreases and also reaches its lowest value at 8.5%. The high concentration of sp^2 C═C bonds in LIG85 aligns with its low sheet resistance. Additionally, LIGs contain a small proportion of characteristic $\pi-\pi^*$ bond component representing the hexagonal carbon lattice, and it slightly increases with increasing laser power. These analyses demonstrate that the designed COSLL successfully yields LIG materials with a sp^2 carbon lattice. The presence of impurity oxygen offers abundant electrochemically active sites. Therefore, LIG75 electrodes, characterized by both rich defect sites and high oxygen content, emerge as the prime candidates for achieving MSCs with larger electrochemical capacitance.

Contact angle tests were conducted to assess changes in surface hydrophilicity before and after laser treatments. As shown in Figure 2l, there is a minimal contact angle of 27.3° between water droplets and the untreated COS/PVA film, indicating a high level of hydrophilicity. However, as the LIG surface approaches the hanging water droplet, it rapidly absorbs the droplet, effectively reducing the contact angle to zero. LIGs generated at various laser power settings exhibit the same exceptional superhydrophilic properties, attributed to their highly porous 3D networks and the presence of polar

https://doi.org/10.1021/acsami.4c02139
ACS Appl. Mater. Interfaces 2024, 16, 35651−35665

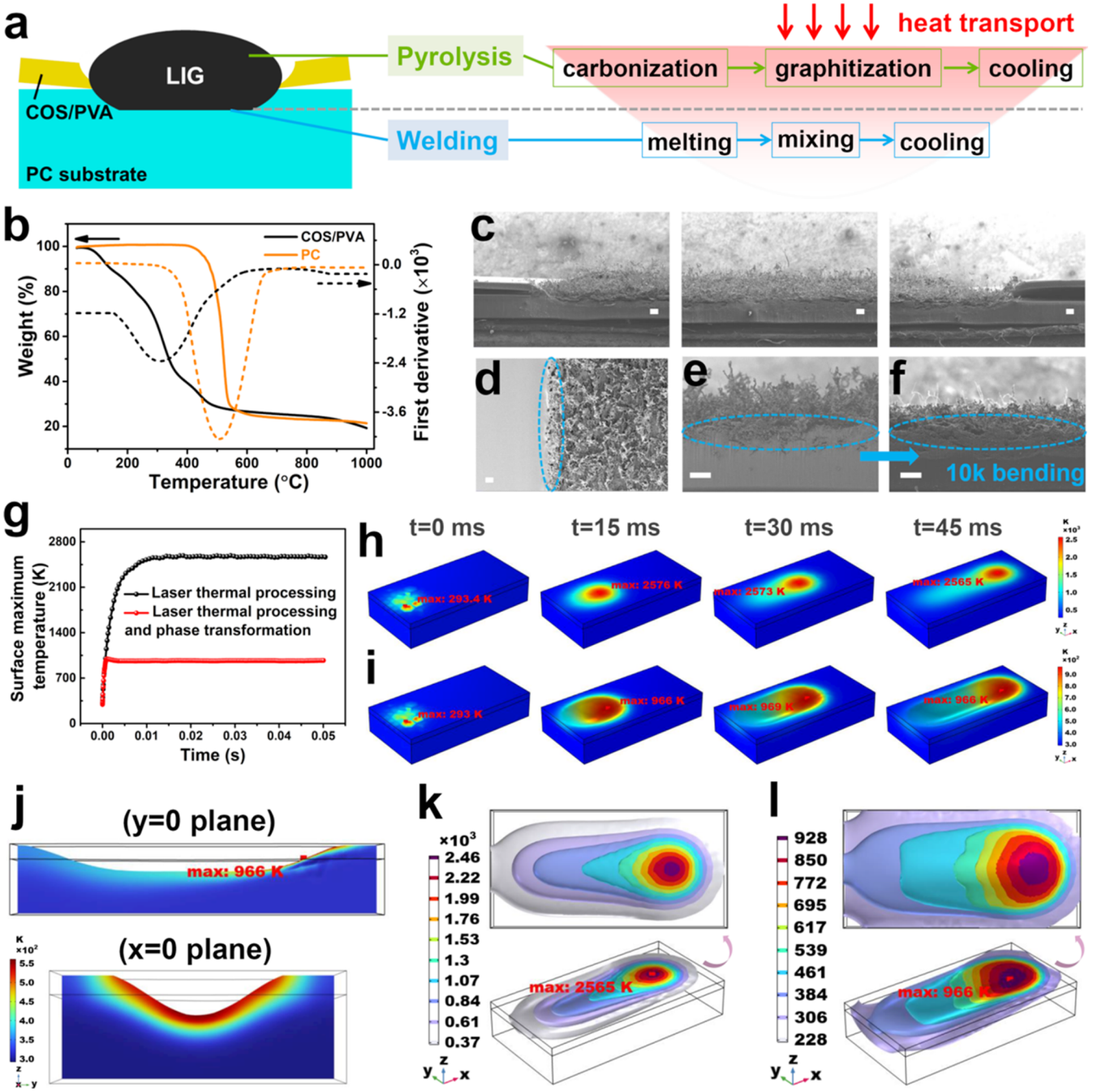


Figure 3. Mechanism of pyrolysis−welding coupled COSLL technology. (a) Schematic illustrations depicting the cross-sectional model and corresponding heat conduction routes for laser pyrolysis and laser welding. (b) TGA curves of COS/PVA and PC. (c) Cross-sectional SEM images of the LIG85/PC composite film with unremoved COS/PVA. (d) Top SEM view of LIG85/PC composite film without COS/PVA remnant. (e, f) High-resolution cross-sectional SEM images of unbent LIG85 and LIG85 after 10,000 bending cycles. (g) Maximum surface temperature versus time curves of two different models under laser treatment. Dynamic simulation states of (h) laser thermal processing and (i) laser thermal processing and phase transition at different times (t = 0, 15, 30, 45 ms). (j) Cross-sectional views of panel (i) at 45 ms, and the legend of the y = 0 plane is the same as that of panel (i). 3D isothermal surface distributions of (k) laser thermal processing and (l) laser thermal processing and phase transition at 45 ms.

oxygen-containing functional groups. The ultrahydrophilic nature of all of these prepared LIGs could facilitate the deep penetration of aqueous gel electrolytes, which is beneficial for enhancing the electrochemical performance of MSCs.

The mechanism of COSLL is further analyzed in detail. As depicted in Figure 3a, a cross-sectional model is established to explain how COS-derived LIGs directly are printed on the PC substrate after laser treatment. When the Gaussian beam is radiated to the upper surface, the transmission of incident laser can be regarded as approximately conforming to the Beer−Lambert Law, and the laser energy decays exponentially as the depth increases. Based on this energy transfer characteristic, the realization of COSLL can be considered to involve two coupling mechanisms, namely, laser pyrolysis and laser welding. The carbon source layer COS/PVA is completely pyrolyzed to target porous LIG materials under intense

https://doi.org/10.1021/acsami.4c02139
ACS Appl. Mater. Interfaces 2024, 16, 35651−35665

photothermal effects, and the generated LIGs are further connected with the PC supporting layer through thermal fusion joining at a relatively low-temperature range. The production of LIG by laser pyrolysis generally involves a process of carbonization, graphenization, and cooling,[51] and is usually thought to be driven by a photothermal reaction. As shown in power-independent Raman spectra (Figure S8b), when the laser power is as low as 3%, the reaction heat can only enable the generation of amorphous carbon, and only when a certain power threshold of 6.0% is reached, graphenization can be finally realized based on carbonization. On the other hand, from the perspective of the plastic substrate, laser welding commonly includes melting, mixing, and cooling. The generated LIGs from the carbon source layer are deeply mixed with the molten pool and form a highly reliable connection interface through van der Waals forces. It is worth noting that part of the PC polymer at the interface will inevitably be decomposed. In addition, it can be seen from Figure S8d that under similar process conditions, as the laser power increases, the high temperature will directly decompose PC into gaseous substances without the generation of visible black carbon materials, which means that the PC substrate does not participate in the formation of target LIGs.

The TGA curves disclose the decomposition temperatures of both COS/PVA and PC films (Figure 3b). The former begins to decompose at a very low temperature of ∼50 °C and follows a violent decomposition at about 300 °C (573 K), while the latter exhibits high thermal stability, which begins to decompose at more than 400 °C (673 K) and has a maximum decomposition rate at ∼500 °C (773 K). In the range of about 200−400 °C (473−673 K), the PC polymer exists in a molten state. After more than 600 °C (873 K), they have highly similar decomposition curves, and their weight retentions are less than 20% when the temperature reaches 1000 °C (1273 K), which implies sufficient pyrolysis. These analyses show that the COS/PVA carbon source layer is extremely prone to pyrolysis after absorbing strong incident laser, while the PC layer has relatively high thermal stability faced with decayed heat energy, affording the basis for effective thermal fusion connection. Cross-sectional SEM images (Figure 3c) provide more intuitive profile information on laser-treated composite films using the COSLL method. It can be seen that the COS/PVA film of about 80 μm is transformed into a LIG layer with a thickness of about 300 μm and it tightly adhered to the PC substrate. On the left and right sides, a clear half-bell heterogeneous interface can be observed, which could contribute to the final scribing of the CO_2 laser beam with Gaussian intensity distribution. In addition, the residual COS/PVA is completely separated from PC by shear stress and does not undergo brittle cracking, which also indicates that the remove process of COSLL is easy to achieve. The top view in Figure 3d shows the fusion boundary between LIGs and PC on the surface. The wrinkled and porous appearance is attributed to the cooling of the PC molten pool and the release of decomposition gas products. To characterize the reliability of LIG welding on a PC substrate, 10,000 cycled bending and recovery tests were performed on LIG/PC composite films with a 5 × 30 mm^2 LIG resistor (Figure S11a,b). High-resolution SEM images (Figure 3d,e) show that after a cyclic bending, the loose surface structure of LIG is significantly detached under continuous bending stress, yet the dense LIG layer with a thickness of approximately 100 μm remains firmly attached to the PC substrate surface. In addition, no observable cracks were detected at the interface between the LIG and PC film, indicating a highly secure laser thermal fusion connection. Furthermore, although long-term and high-intensity bending impacts caused a certain degree of irreversible damage to the LIG network, the resistors still maintain good electrical conductivity (Figure S11c).

3D numerical models were constructed based on a COS/PVA PC bilayer film to simulate the temperature distribution, morphology change, and stress variation in the COSLL process using COMSOL Multiphysics software. In Figure 3g,h, when a 10.6 μm laser with a power of 8.5% is used to radiate the surface, tremendous energy drives the interactions of the incident laser and materials, and the maximum surface temperature reaches more than 2500 K in a very short time (about 10 ms). This large temperature can completely facilitate full pyrolysis of the carbon source layer. Actual pyrolysis involves complex physical and chemical reactions (Figure S12a),[65] primarily reflected in the volatilization of plasma and generation of LIG. Therefore, the simulation model is optimized by adding a phase transition process, assuming that when the temperature exceeds the thermal ablation threshold, the materials will completely change from solid to gas with the corresponding mass loss. The results in Figure 3g,i show that after laser-engraving, the surface of the bilayer film forms a distinct thermal erosion groove, and the maximum surface temperature of 966 K is already below the decomposition boundary of 1273 K, no longer able to support sufficient pyrolysis of the COS/PVA layer. It can be further observed from the cross-sectional view (Figure 3j, y = 0 plane) that near the processing site (t = 45 ms), due to the phase change taking away a large amount of heat, high temperatures exceeding 900 K only exist in very thin areas, and the temperature sharply decays along the z-axis direction. In the x = 0 plane (Figure 3j), corresponding to t = 25 ms, where the light source has left, it can be seen that the maximum surface temperature of the PC substrate is maintained at about 550 K, aligning with the temperature range (about 473−673 K) that can form a molten pool. The cross-sectional shape is also consistent with the observed SEM images (Figure 3c). In the top view of the 3D isothermal distribution map (Figure 3k), it can be seen that laser thermal processing will form a teardrop-shaped area exceeding 1273 K, allowing the COS/PVA layer to be fully pyrolyzed. After the material sublimates, a trapezoidal area with a temperature range of 473−673 K will be formed, leaving the PC substrate in a molten state (Figure 3l). Importantly, along the x-direction, the trapezoidal area melting temperature zone always lags behind the teardrop-shaped pyrolysis temperature zone, meaning that pyrolysis and welding can occur in an orderly manner, which is fundamental for their effective coupling. Additionally, laser ablation will also lead to large thermal stress (Figure S12d), which is conducive to the removal step in the COSLL process because the thermal expansion coefficients of COS/PVA and PC are not well-matched. These finite element simulations for laser thermal processing and phase transition provide a more detailed theoretical basis for the pyrolysis−welding coupled mechanism of COSLL.

The conventional DLW technology to manufacture LIG also relies on a pyrolysis−welding coupled mechanism (Figure S4). Taking PI film as an example, part of the surface is transformed into target LIG materials via laser pyrolysis, and the generated LIGs further adhere to the nonpyrolyzed inner PI structure through thermal fusion bonding.[66] In this case, PI acts as both

https://doi.org/10.1021/acsami.4c02139
ACS Appl. Mater. Interfaces 2024, 16, 35651−35665

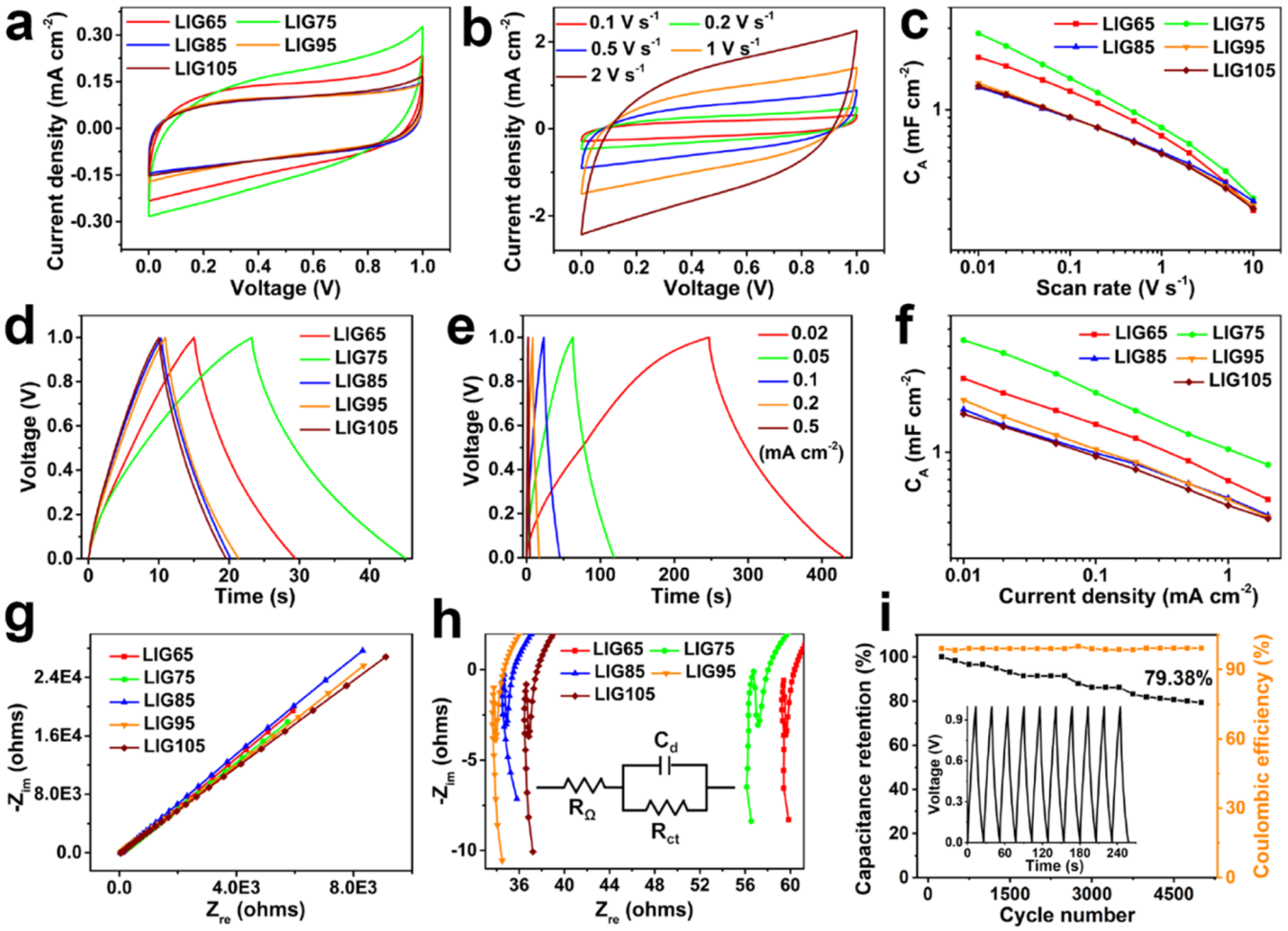


Figure 4. Electrochemical characterizations of MSCs featuring eight-interdigitated electrodes prepared at five different laser powers (6.5−10.5%) in a PVA/H_2SO_4 gel electrolyte. (a) CV curves of MSCs measured at a scan rate of 0.1 V s^{-1}. (b) CV curves of MSC with LIG75 electrodes measured at different scan rates. (c) CV curve-derived areal capacitance (C_A) versus scan rate for five laser power-independent LIG electrodes. (d) GCD curves of MSCs measured at a current density of 0.1 mA cm^{-2}. (e) GCD curves of MSC with LIG75 electrodes measured at different current densities. (f) GCD curve-derived C_A versus current density for five laser power-independent LIG electrodes. (g) Nyquist plot and (h) zoomed-in Nyquist plot of LIG MSCs, with the inset of panel (h) depicting the equivalent circuit model. (i) Cycling stability of LIG75 MSC measured at a current density of 0.2 mA cm^{-2}, with the inset showing the last 10 GCD cycles.

a carbon source layer and a support layer. Compared with DLW, laser lithography has the advantage of in situ transfer of LIG generated in the carbon source layer to another selected support layer, which is essential for the efficient use of carbon source materials that are not self-supporting, such as chitosan-based substrates. However, the implementation of laser lithography is extremely challenging and requires a high degree of matching between the carbon source layer and the support layer. On one hand, laser pyrolysis involves very complex physicochemical processes, and the addition of heterogeneous substrates may make the pyrolysis products uncertain, although the carbon source layer can originally be graphenized. On the other hand, when the compatibility of the material is very low, the generated LIG is easy to fall off the substrate due to the absence of a strong melt connection, which is very unfavorable to device preparation. Therefore, the successful practice of COSLL is exciting and paves a new way to green and sustainable LIG electronics based on eco-friendly chitosan-class materials. It is also noteworthy that the preparation of LIG on PC film using the COSLL method exhibits remarkable processability. As depicted in Figure S1, the CO_2 laser offers a broad spectrum of precisely adjustable parameters, facilitating the exploration of optimal processing conditions. In this investigation, laser power stands as the singular regulated parameter for controlling LIG formation, while other process parameters remain constant. As illustrated in Figure S8, a mere 3% increase in duty cycle within the range of 3−12% results in notable variations in morphology, sheet resistance, and Raman spectra across different batches of LIGs. Consequently, at specific laser power settings, the resulting LIGs exhibit relatively stable physical and chemical properties, allowing for rapid evaluation through simple electrical or optical tests. This highly processable characteristic of COSLL greatly facilitates the production of LIG devices in large quantities.

As previously discussed, LIG derived from COS showcases porous structures, remarkably low sheet resistances, and excellent superhydrophilic properties, rendering it an exemplary material for high-performance MSCs. Leveraging the COSLL technique, eight-folded LIG in-plane interdigital electrodes with a total area of 0.48 cm^2 were fabricated on a PC film, utilizing a laser power range of 6.5−10.5%. Subsequently, these electrodes were integrated into all-solid on-chip MSCs employing PVA/H_2SO_4 gel electrolytes (Figure S13) and the electrochemical performance of the resulting

https://doi.org/10.1021/acsami.4c02139
ACS Appl. Mater. Interfaces 2024, 16, 35651−35665

MSCs is elucidated in Figure 4. CV curves (Figure 4a) illustrate that the manufactured MSCs, with LIG electrodes produced at varying laser powers exhibit a symmetrical quasi-rectangular response indicative of typical electric double-layer capacitor (EDLC) charge−discharge behavior. This EDLC behavior is further underscored by the symmetrical quasi-rectangular CV curves of LIG75 at different scan rates (Figure 4b). Areal capacitances of laser power-dependent LIG electrodes against scan rates are depicted in Figure 4c. Notably, LIG85−LIG105 electrodes present relatively smaller and nearly equivalent areal capacitances across a broad spectrum of scan rates, ranging from 0.01 to 5 V s^{-1}, while LIG65 and LIG75 demonstrate superior performance. The electrochemical performance of LIG electrodes appears to follow an increasing-then-decreasing trend with the enhancement of laser power, exhibiting a capacitance cutoff at higher powers (8.5−10.5%). Among these, LIG75 electrodes stand out, showcasing the highest areal capacitance of 2.8 mF cm^{-2} at a scan rate of 0.01 V s^{-1}. This remarkable achievement can primarily be attributed to the abundance of defect-state electrochemically active sites, as evidenced by the highest I_D/I_G ratio in Figure 2i, setting them apart from other LIG counterparts. Furthermore, the relatively high oxygen content of LIG75 (Table S2) plays a significant role in enhancing both the electron transport and interface properties of the graphene structure, thereby further augmenting its electrochemical performance. However, it is noteworthy that with increasing scan rates, LIG65 and LIG75 electrodes exhibit a faster rate of capacitance decay. This is likely due to their elevated equivalent series resistance (ESR) and a more restricted kinetic transmission induced by defect sites, indicating the delicate balance between power enhancement and electrochemical performance.

GCD tests were performed for LIG electrodes produced at various laser powers through chronopotentiometry, and corresponding areal capacitances were calculated. In the complete charge and discharge cycles, all LIG electrodes exhibit highly symmetrical GCD curves (Figure 4d), indicative of robust EDLC behavior and excellent Coulombic efficiency. The GCD results for LIG75 electrodes further demonstrate the maintenance of superior EDLC properties across different current densities (Figure 4e). As illustrated in Figure 4d,f, LIG electrodes printed at lower laser powers (6.5 and 7.5%) exhibit superior areal capacitances compared to their counterparts obtained at higher laser powers (8.5−10.5%). Notably, LIG85−LIG105 electrodes exhibit almost identical attenuation curves as the current density increases. The maximum areal capacitance for LIG electrodes at different laser powers, obtained at a current density of 0.01 mA cm^{-2}, are 2.6, 4.3, 1.8, 2.0, and 1.7 mF cm^{-2}, with LIG75 achieving the peak value of 4.3 mF cm^{-2}. The maximum areal capacitance is comparable to or higher than that of previously developed on-chip MSCs based on LIG interdigitated electrodes derived from various carbonaceous precursors, such as classical PI,[23] graphite oxide,[67] lignin,[63] and metal−organic framework,[68] as summarized in Table S3. The trends in areal capacitance from the GCD curves align closely with those from the CV curves, emphasizing the pivotal role of defect-state graphene lattice in capacitance regulation again. It is worth noting that LIG75 electrodes exhibit a higher areal capacitance in the chronopotentiometry test compared to the CV measurement, owing to the longer test duration and increased charge accumulation. Based on the GCD-derived areal capacitances, energy−power characteristic curves of LIG MSCs were further calculated and plotted in Figure S14. The Ragone plots exhibit excellent linearity, signifying that, irrespective of the applied laser power in COSLL, LIG MSCs consistently demonstrate well-balanced performance across various power and energy requirements. Notably, LIG75 electrodes exhibit a higher areal energy density than their counterparts at the same areal power density, aligning with the variation trend of GCD-based areal capacitance. Additionally, when discharging with the maximum power density of 1 mW cm^{-2}, the energy density of the MSCs are 0.075, 0.118, 0.061, 0.060, and 0.058 μWh cm^{-2} for LIG65−LIG105 electrodes.

EIS analyses provide insights into the influence of laser power on the electrochemical performance of LIG-based MSCs. Nyquist plots (Figure 4g) illustrate distinct capacitive linear curves for all MSCs. Notably, LIG65 and LIG75 electrodes, with lower $-Z_{im}$ values, exhibit significantly larger equivalent capacitances compared to their LIG85−LIG105 counterparts in the low-frequency region because of their low capacitive reactance (Figure S15). Further scrutiny in the enlarged Nyquist plots (Figure 4h) highlights the EIS characteristics of LIG MSCs in the high-frequency region, with the inset revealing a simplified equivalent RC circuit model. LIG65 and LIG75 show relatively large ESR values of 59.9 and 56.5 Ω, respectively, while LIG85−LIG105 exhibit smaller ESRs of 35.8, 34.5, and 37.2 Ω. This trend aligns consistently with the sheet resistance measurement presented in Figure 2j. This result demonstrates that high-quality and low-defect electrodes (LIG85−LIG105 included) can lower the ESR of the device but simultaneously inhibit the improvement of electrochemical performance. Additionally, all MSCs demonstrate minimal charge transfer resistance (R_{ct}), indicative of highly efficient charge and discharge behavior. Bode diagrams (Figure S16) further emphasize the favorable capacitive character of MSCs in the low-frequency region, enabling effective DC energy storage. As the frequency increases, the impedance values decrease rapidly, maintaining notable resistivity within a broad high-frequency range. At a phase angle of −45°, their cutoff frequency range is observed between 6 and 18 Hz. Through comprehensive analyses encompassing CV, GCD, and EIS techniques, the findings highlight the challenge of achieving both significant areal capacitance and low ESR simultaneously at a specific laser power. This challenge stems from the inherent constraints imposed by defect-state sites and heteroatomic functional groups within LIG networks. Overall, LIG75 with highest capacitance density remains the most competitive candidate for fabricating high-performance on-chip MSCs despite its relatively elevated ESR.

Long-cycle GCD test was further conducted to assess work stability and performance retention of LIG75 MSC. As depicted in Figure 4i, even after 5000 constant-current charge−discharge cycles, the device still retains capacitance retention of about 80% with Coulombic efficiency of nearly 100%, showcasing remarkable long-term cycle stability and consistent EDLC characteristics. The long-cyclic bending durability test of the LIG75 MSC device was also conducted (Figure S17a). When considering the curved device as an arc, the calculated bending radius and central angle approximate 10.30 mm and 167°, respectively. However, in reality, the curvature is much more pronounced than that of a simple arc. The capacitance retention during mechanical bending was evaluated through CV characterization at a scan rate of 1 V s^{-1}

https://doi.org/10.1021/acsami.4c02139
ACS Appl. Mater. Interfaces 2024, 16, 35651−35665

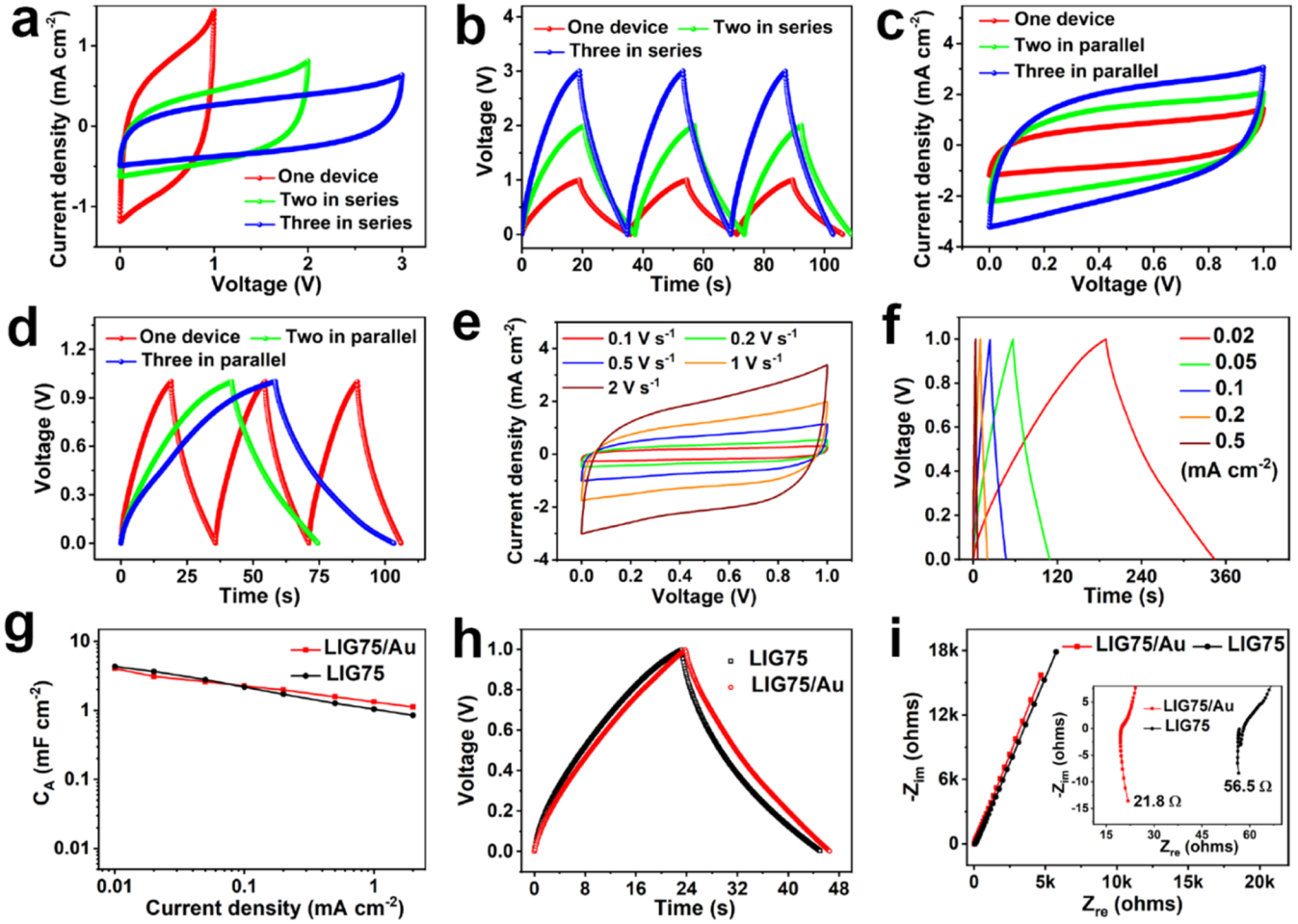


Figure 5. Electrochemical evaluations of integrated LIG75 MSCs and single LIG75/Au MSC. CV curves of LIG75 MSCs connected (a) in series and (b) in parallel, both recorded at a scan rate of 1 V s^{-1}. GCD profiles of LIG75 MSCs connected (c) in series and (d) in parallel, measured at a current density of 0.1 mA cm^{-2}. (e) CV curves of LIG75/Au MSC measured at different scan rates. (f) GCD profiles of LIG75/Au MSC measured at different current densities. (g) Areal capacitance comparison between LIG75 and LIG75/Au MSCs obtained from GCD tests. (h) GCD curves of LIG75 MSC and LIG75/Au MSC, measured at a current density of 0.1 mA cm^{-2}. (i) Nyquist plots and zoomed-in Nyquist plots (inset) for LIG75 and LIG75/Au MSCs.

(Figure S17b,c). The results indicate that the device maintains a remarkably stable electrochemical performance even during high-strength bending cycles of up to 2000 cycles. Upon exceeding 3000 bends, the substrate may experience plastic fracture due to mechanical stress. Nevertheless, prior to fracture, the device can still retain 98.66% of its performance. This resilience suggests that the as-prepared LIG MSCs possess excellent bending durability, which can be attributed to the reliable fusion joining of LIG electrodes on the PC substrate and the robust packaging structure of MSC devices. Furthermore, the bending resistance underscores the promising potential of LIG MSCs for applications in flexible electronics or wearable electronics.

Moreover, LIG interdigital electrodes can be efficiently produced in batches on the target substrate using COSLL technology (Figure S3b), enabling large-scale integration of LIG MSCs through series and parallel connections as per actual requirements. The highly symmetrical quasi-rectangular CV curves in Figure 5a demonstrate that devices connected in series maintain good EDLC properties. Series connection proportionally widens the voltage window of the LIG MSC module compared to the individual device. The GCD curves (Figure 5b) show that, at the same current density, series-connected LIG MSCs achieve similar charge and discharge behaviors at a higher operating voltage than a single device, which is beneficial for end loads that require higher input voltages. EIS analyses (Figure S18a,b) further reveal that the areal capacitance decreases proportionally to that of a single device as the number of series MSCs increases, while the ESR increases correspondingly. Parallel connection, as depicted in Figure 5c, does not change the voltage window of 1 V, but significantly increases the capacitance value while maintaining excellent EDLC characteristics. The GCD profiles (Figure 5d) demonstrate that at an operating voltage of 1 V, as the number of parallel devices increases, the discharge time proportionally increases, extending the time to drive the target load. EIS diagrams (Figure S18c,d) reveal that parallel connection not only increases the capacitance proportionally but also reduces the ESR. Notably, when three MSCs are connected in parallel, the charge transfer resistance is significantly suppressed. These analyses underscore that both the operating voltage and capacitance of LIG MSCs can be tailored through series-parallel integration, offering great flexibility for their application in flexible power systems.

Thanks to the high compatibility between COSLL technology and the CMOS metal deposition process,

https://doi.org/10.1021/acsami.4c02139
ACS Appl. Mater. Interfaces 2024, 16, 35651−35665

LIG75/Au electrodes (Figure S19) and corresponding MSCs were prepared. SEM images in Figure S20 reveal that at a resolution of 10 μm, the morphology of the gold-plated sample shows no significant change, displaying a loose and irregular structure similar to that of pure LIG75. However, higher-resolution SEM images (Figure S20b,e) demonstrate that electron beam evaporation of the gold target results in tightly attached clusters of gold particles on the surface of 3D LIGs. These gold particles can exceed 200 nm in length, and their cluster morphology is typically random (as observed in Figure S20d,e). Furthermore, due to the shielding effect of the surface structure, the formation of gold particles in the bottom region is relatively limited (as shown in Figure S20e). As depicted in Figure S21, the attachment of metallic gold particles significantly reduces the sheet resistance of LIG samples from 14.2 to 1.8 Ω sq^{-1}, thus greatly enhancing the electron transport capacity. These results suggest that additional metal deposition on the surface of LIG may offer a convenient solution to further decrease the ESR of LIG MSCs.

The electrochemical properties of LIG75/Au MSCs were further characterized. As depicted in the CV curves of Figure 5e, LIG75/Au MSCs maintain a good quasi-triangular configuration at different scan rates similar to the unmodified LIG75 analogue, indicating a typical EDLC mechanism. Highly symmetrical triangle GCD curves at different current densities (Figure 5f) also reveal the good charge−discharge EDLC behavior and excellent Coulombic efficiency of Au-coated MSCs. The plots of areal capacitance as a function of current density in Figure 5g provide a more comprehensive view of the impact of Au decoration. It can be seen that, within the current density range from 0.01 to 2 mA cm^{-2}, the areal capacitance of LIG75/Au MSCs exhibits an almost identical trend to that of its LIG75 counterparts, and the Au-loaded device can reach a highest areal capacitance of 4.1 mF cm^{-2} at 0.01 mA cm^{-2}, comparable to that of Au-free LIG75 MSC (4.3 mF cm^{-2}). These results suggest that the deposition of gold does not enhance the electrochemical performance behavior of MSCs and the mechanism for storing electricity has not changed. The main reason for this phenomenon is that the electrochemical performance of LIG75/Au MSCs is primarily dominated by the hierarchically porous LIG network, and the loading of gold on the surface of 3D LIG is merely equivalent to the addition of a layer of metal collector with higher electrical conductivity. Although the loading of Au does not improve the areal capacitance, the capacitance decay rate of LIG75/Au is relatively weak as the current density increases (Figure 5g). It can also be seen from Figure 5h that the gold-coating may help reduce the polarization effect of the electrode, making the discharge process of the device more uniform and stable, resulting in a discharge curve closer to the triangular side. In addition, the gold-coating significantly reduces both R_{ct} and ESR, and the ESR of the LIG75/Au MSC can be reduced to 21.8 Ω (Figure 5i), which is beneficial to enhance the maximum power point for external loads. These analyses underscore that a convenient and compatible metal deposition process can help further reduce the internal resistance while maintaining the electrochemical performance of COSLL-prepared LIG MSCs.

CONCLUSIONS

In conclusion, based on eco-friendly chitosan-class biomass materials, we have successfully developed a convenient COSLL technology for the preparation of hierarchically porous LIG electrodes and flexible on-chip MSCs. The COSLL method, involving a straightforward one-step CO_2 laser treatment and a dry-transferable peel-off process, enables the direct printing of LIG electrodes with arbitrary patterns on diverse engineering plastic substrates. The pyrolysis−welding coupled mechanism underlines the foundation of COSLL originating from the volatile pyrolysis of the carbon source layer and the thermal fusion joining of the generated LIGs to the plastic substrate. Finite element simulations substantiate that the temperature distribution during laser thermal processing and phase transition aligns with experimental observations, and extended long-cycle bending tests further attest to the highly reliable bonding of LIGs on heterogeneous substrates. The resulting LIG materials showcase intricate 3D porous structures, coupled with abundant defect-state electrochemically active sites, and a superhydrophilic surface. Remarkably, the sheet resistance of LIGs can reach as low as 6.3 Ω sq^{-1}. Capitalizing on these exceptional attributes, LIG MSCs prepared by COSLL demonstrate substantial areal capacitance exceeding 4 mF cm^{-2}, comparable to PI-derived LIG MSCs. With the incorporation of an additional CMOS and MEMS-compatible film deposition process, it can also significantly reduce the internal resistance of the device while preserving its electrochemical performance. The flexible LIG MSCs also exhibit robust bending performance and possess large-scale series-parallel integration capabilities, making them well-suited for various application scenarios in flexible electronics. This work amalgamates both material and process innovation, offering a novel approach for the fabrication of flexible on-chip LIG MSCs and other advanced LIG devices.

ASSOCIATED CONTENT

Supporting Information

The Supporting Information is available free of charge at https://pubs.acs.org/doi/10.1021/acsami.4c02139.

Finite element analysis method; formula of crystallized COS; LIG patterns on several plastic substrates achieved by the COSLL method; comparison of conventional lithography, DLW, and COSLL method; SEM and TEM images of LIG samples; Raman spectrum of COS/PVA; Raman spectra and sheet resistance of LIGs; Raman peak positions of LIGs; survey XPS spectra and corresponding elemental contents of COS/PVA and LIGs; deconvoluted C 1s XPS spectra of COS/PVA and LIGs; laser fusion joining reliability test of LIG on the PC film; laser thermal processing and phase transition simulation results; LIG interdigitated electrode structure design of MSCs; comparison of on-chip LIG MSCs based on different carbonaceous precursors; areal Ragone plots of LIG MSCs; Randless equivalent circuit model of MSCs; Bode plots of LIG MSCs; bending cycle performance of LIG MSC; Nyquist plots of series and parallel LIG MSCs; optical photographs of LIG/Au electrodes; SEM images of LIG/Au sample; and sheet resistance of LIG and LIG/Au (PDF)

AUTHOR INFORMATION

Corresponding Author

Huaiyu Ye − *School of Microelectronics, Southern University of Science and Technology, Shenzhen 518055, China; Faculty of EEMCS, Delft University of Technology, 2628 CD Delft, The*

https://doi.org/10.1021/acsami.4c02139
ACS Appl. Mater. Interfaces 2024, 16, 35651−35665

Netherlands; orcid.org/0000-0002-0385-4728;
Email: h.ye@tudelft.nl

Authors

Qian-Ming Huang − *Harbin Institute of Technology, Harbin 150001, China; School of Microelectronics, Southern University of Science and Technology, Shenzhen 518055, China*

Huiru Yang − *Harbin Institute of Technology, Harbin 150001, China; School of Microelectronics, Southern University of Science and Technology, Shenzhen 518055, China*

Shaogang Wang − *School of Microelectronics, Southern University of Science and Technology, Shenzhen 518055, China; Faculty of EEMCS, Delft University of Technology, 2628 CD Delft, The Netherlands*

Xu Liu − *School of Microelectronics, Southern University of Science and Technology, Shenzhen 518055, China; Faculty of EEMCS, Delft University of Technology, 2628 CD Delft, The Netherlands*

Chunjian Tan − *School of Microelectronics, Southern University of Science and Technology, Shenzhen 518055, China; Faculty of EEMCS, Delft University of Technology, 2628 CD Delft, The Netherlands*

Qihang Zong − *School of Microelectronics, Southern University of Science and Technology, Shenzhen 518055, China*

Chenshan Gao − *School of Microelectronics, Southern University of Science and Technology, Shenzhen 518055, China*

Shizhen Li − *School of Microelectronics, Southern University of Science and Technology, Shenzhen 518055, China*

Paddy French − *Faculty of EEMCS, Delft University of Technology, 2628 CD Delft, The Netherlands*

Guoqi Zhang − *Faculty of EEMCS, Delft University of Technology, 2628 CD Delft, The Netherlands*

Complete contact information is available at: https://pubs.acs.org/10.1021/acsami.4c02139

Author Contributions

Q.-M.H. designed and performed all of the experiments, analyzed relative data, and wrote the manuscript. H.Y., S.W., X.L., C.T., Q.Z., C.G., and S.L. provided plenty of constructive ideas and valuable discussions. H.Y., G.Z., and P.F. provided guidance to the research. All authors have given approval to the final version of the manuscript.

Notes

The authors declare no competing financial interest.

■ ACKNOWLEDGMENTS

This work was supported by the Guangdong Basic and Applied Basic Research Foundation (2023B1515120090), the Shenzhen Major Science and Technology Projects (KJZD20230923114710022), the National Key R&D Program of China (2018YFE0204600), the Shenzhen Fundamental Research Program (JCYJ20200109140822796), the Joint Lab of Advanced Situation Awareness, the Joint Lab of Advanced Packaging Technology, and the Joint Lab of Advanced Packaging and Testing Technology of Integrated Circuits. The authors thank Professor Kwai Hei Li's group for their help in contact angle measurements.

■ REFERENCES

(1) Dubal, D. P.; Chodankar, N. R.; Kim, D.-H.; Gomez-Romero, P. Towards Flexible Solid-State Supercapacitors for Smart and Wearable Electronics. *Chem. Soc. Rev.* **2018**, *47*, 2065−2129.

(2) Zhu, Q.; Zhao, D.; Cheng, M.; Zhou, J.; Owusu, K. A.; Mai, L.; Yu, Y. A New View of Supercapacitors: Integrated Supercapacitors. *Adv. Energy Mater.* **2019**, *9*, No. 1901081.

(3) Cao, X.; Xiong, Y.; Sun, J.; Xie, X.; Sun, Q.; Wang, Z. L. Multidiscipline Applications of Triboelectric Nanogenerators for the Intelligent Era of Internet of Things. *Nano-Micro Lett.* **2022**, *15*, No. 14.

(4) Hu, M.; Zhang, H.; Hu, T.; Fan, B.; Wang, X.; Li, Z. Emerging 2D MXenes for Supercapacitors: Status, Challenges and Prospects. *Chem. Soc. Rev.* **2020**, *49*, 6666−6693.

(5) Noori, A.; El-Kady, M. F.; Rahmanifar, M. S.; Kaner, R. B.; Mousavi, M. F. Towards Establishing Standard Performance Metrics for Batteries, Supercapacitors and Beyond. *Chem. Soc. Rev.* **2019**, *48*, 1272−1341.

(6) Wang, F.; Wu, X.; Yuan, X.; Liu, Z.; Zhang, Y.; Fu, L.; Zhu, Y.; Zhou, Q.; Wu, Y.; Huang, W. Latest Advances in Supercapacitors: from New Electrode Materials to Novel Device Designs. *Chem. Soc. Rev.* **2017**, *46*, 6816−6854.

(7) Wang, Y.; Song, Y.; Xia, Y. Electrochemical Capacitors: Mechanism, Materials, Systems, Characterization and Applications. *Chem. Soc. Rev.* **2016**, *45*, 5925−5950.

(8) Lv, J.; Yin, L.; Chen, X.; Jeerapan, I.; Silva, C. A.; Li, Y.; Le, M.; Lin, Z.; Wang, L.; Trifonov, A.; Xu, S.; Cosnier, S.; Wang, J. Wearable Biosupercapacitor: Harvesting and Storing Energy from Sweat. *Adv. Funct. Mater.* **2021**, *31*, No. 2102915.

(9) Wang, Y.; Yang, Y.; Wang, Z. L. Triboelectric Nanogenerators as Flexible Power Sources. *npj Flexible Electron.* **2017**, *1*, No. 10.

(10) Shao, Y.; El-Kady, M. F.; Sun, J.; Li, Y.; Zhang, Q.; Zhu, M.; Wang, H.; Dunn, B.; Kaner, R. B. Design and Mechanisms of Asymmetric Supercapacitors. *Chem. Rev.* **2018**, *118*, 9233−9280.

(11) Salanne, M.; Rotenberg, B.; Naoi, K.; Kaneko, K.; Taberna, P. L.; Grey, C. P.; Dunn, B.; Simon, P. Efficient Storage Mechanisms for Building Better Supercapacitors. *Nat. Energy* **2016**, *1*, No. 16070.

(12) Liu, L.; Niu, Z.; Chen, J. Unconventional Supercapacitors from Nanocarbon-Based Electrode Materials to Device Configurations. *Chem. Soc. Rev.* **2016**, *45*, 4340−4363.

(13) Zhang, Y.; Mei, H.-x.; Cao, Y.; Yan, X.-h.; Yan, J.; Gao, H.-l.; Luo, H.-w.; Wang, S.-w.; Jia, X.-d.; Kachalova, L.; Yang, J.; Xue, S.-c.; Zhou, C.-g.; Wang, L.-x.; Gui, Y.-h. Recent Advances and Challenges of Electrode Materials for Flexible Supercapacitors. *Coord. Chem. Rev.* **2021**, *438*, No. 213910.

(14) Xie, P.; Yuan, W.; Liu, X.; Peng, Y.; Yin, Y.; Li, Y.; Wu, Z. Advanced Carbon Nanomaterials for State-of-the-Art Flexible Supercapacitors. *Energy Storage Mater.* **2021**, *36*, 56−76.

(15) Keum, K.; Kim, J. W.; Hong, S. Y.; Son, J. G.; Lee, S. S.; Ha, J. S. Flexible/Stretchable Supercapacitors with Novel Functionality for Wearable Electronics. *Adv. Mater.* **2020**, *32*, No. 2002180.

(16) Jia, R.; Shen, G.; Qu, F.; Chen, D. Flexible On-Chip Micro-Supercapacitors: Efficient Power Units for Wearable Electronics. *Energy Storage Mater.* **2020**, *27*, 169−186.

(17) Fang, C.; Tong, T.; Bu, T.; Cao, Y.; Xu, S.; Qi, Y.; Zhang, C. Overview of Power Management for Triboelectric Nanogenerators. *Adv. Intell. Syst.* **2020**, *2*, No. 1900129.

(18) Kyerematen, N. A.; Brousse, T.; Pech, D. Microsupercapacitors as Miniaturized Energy-Storage Components for On-Chip Electronics. *Nat. Nanotechnol.* **2017**, *12*, 7−15.

(19) Zhang, Y. Z.; Wang, Y.; Cheng, T.; Yao, L. Q.; Li, X.; Lai, W. Y.; Huang, W. Printed Supercapacitors: Materials, Printing, and Applications. *Chem. Soc. Rev.* **2019**, *48*, 3229−3264.

(20) Benzigar, M. R.; Dasireddy, V. D. B. C.; Guan, X.; Wu, T.; Liu, G. Advances on Emerging Materials for Flexible Supercapacitors: Current Trends and Beyond. *Adv. Funct. Mater.* **2020**, *30*, No. 2002993.

(21) Wu, D.-Y.; Shao, J.-J. Graphene-Based Flexible All-Solid-State Supercapacitors. *Mater. Chem. Front.* **2021**, *5*, 557−583.

(22) Wang, Y.; Wu, X.; Han, Y.; Li, T. Flexible Supercapacitors: Overview and Outlooks. *J. Energy Storage* **2021**, *42*, No. 103053.
(23) Lin, J.; Peng, Z.; Liu, Y.; Ruiz-Zepeda, F.; Ye, R.; Samuel, E. L.; Yacaman, M. J.; Yakobson, B. I.; Tour, J. M. Laser-Induced Porous Graphene Films from Commercial Polymers. *Nat. Commun.* **2014**, *5*, No. 5714.
(24) Liu, C.; Liang, H.; Wu, D.; Lu, X.; Wang, Q. Direct Semiconductor Laser Writing of Few-Layer Graphene Polyhedra Networks for Flexible Solid-State Supercapacitor. *Adv. Electron. Mater.* **2018**, *4*, No. 1800092.
(25) Lamberti, A.; Clerici, F.; Fontana, M.; Scaltrito, L. A Highly Stretchable Supercapacitor Using Laser-Induced Graphene Electrodes onto Elastomeric Substrate. *Adv. Energy Mater.* **2016**, *6*, No. 1600050.
(26) Le, T. S. D.; Phan, H. P.; Kwon, S.; Park, S.; Jung, Y.; Min, J.; Chun, B. J.; Yoon, H.; Ko, S. H.; Kim, S. W.; Kim, Y. J. Recent Advances in Laser-Induced Graphene: Mechanism, Fabrication, Properties, and Applications in Flexible Electronics. *Adv. Funct. Mater.* **2022**, No. 2205158.
(27) Yuan, Y.; Li, X.; Jiang, L.; Liang, M.; Zhang, X.; Wu, S.; Wu, J.; Tian, M.; Zhao, Y.; Qu, L. Laser Maskless Fast Patterning for Multitype Microsupercapacitors. *Nat. Commun.* **2023**, *14*, No. 3967.
(28) Yuan, Y.; Jiang, L.; Li, X.; Zuo, P.; Xu, C.; Tian, M.; Zhang, X.; Wang, S.; Lu, B.; Shao, C.; Zhao, B.; Zhang, J.; Qu, L.; Cui, T. Laser Photonic-Reduction Stamping for Graphene-Based Micro-Supercapacitors: Ultrafast Fabrication. *Nat. Commun.* **2020**, *11*, No. 6185.
(29) Liu, H.; Sun, Z.; Chen, Y.; Zhang, W.; Chen, X.; Wong, C. P. Laser Processing of Flexible In-Plane Micro-supercapacitors: Progresses in Advanced Manufacturing of Nanostructured Electrodes. *ACS Nano* **2022**, *16*, 10088−10129.
(30) Ye, R.; James, D. K.; Tour, J. M. Laser-Induced Graphene. *Acc. Chem. Res.* **2018**, *51*, 1609−1620.
(31) Zhao, L.; Liu, Z.; Chen, D.; Liu, F.; Yang, Z.; Li, X.; Yu, H.; Liu, H.; Zhou, W. Laser Synthesis and Microfabrication of Micro/Nanostructured Materials Toward Energy Conversion and Storage. *Nano-Micro Lett.* **2021**, *13*, No. 49.
(32) Kumar, R.; del Pino, A. P.; Sahoo, S.; Singh, R. K.; Tan, W. K.; Kar, K. K.; Matsuda, A.; Joanni, E. Laser Processing of Graphene and Related Materials for Energy Storage: State of the Art and Future Prospects. *Prog. Energy Combust. Sci.* **2022**, *91*, No. 100981.
(33) Liu, H.; Xie, Y.; Liu, J.; Moon, K.-s.; Lu, L.; Lin, Z.; Yuan, W.; Shen, C.; Zang, X.; Lin, L.; Tang, Y.; Wong, C.-P. Laser-Induced and KOH-Activated 3D Graphene: A Flexible Activated Electrode Fabricated via Direct Laser Writing for In-Plane Micro-Supercapacitors. *Chem. Eng. J.* **2020**, *393*, No. 124672.
(34) Guo, H.; Qiao, M.; Yan, J.; Jiang, L.; Yu, J.; Li, J.; Deng, S.; Qu, L. Fabrication of Hybrid Supercapacitor by $MoCl_5$ Precursor-Assisted Carbonization with Ultrafast Laser for Improved Capacitance Performance. *Adv. Funct. Mater.* **2023**, *33*, No. 2213514.
(35) Li, L.; Zhang, J.; Peng, Z.; Li, Y.; Gao, C.; Ji, Y.; Ye, R.; Kim, N. D.; Zhong, Q.; Yang, Y.; Fei, H.; Ruan, G.; Tour, J. M. High-Performance Pseudocapacitive Microsupercapacitors from Laser-Induced Graphene. *Adv. Mater.* **2016**, *28*, 838−845.
(36) Ye, R.; Peng, Z.; Wang, T.; Xu, Y.; Zhang, J.; Li, Y.; Nilewski, L. G.; Lin, J.; Tour, J. M. In Situ Formation of Metal Oxide Nanocrystals Embedded in Laser-Induced Graphene. *ACS Nano* **2015**, *9*, 9244−9251.
(37) Ye, R.; James, D. K.; Tour, J. M. Laser-Induced Graphene: From Discovery to Translation. *Adv. Mater.* **2019**, *31*, No. 1803621.
(38) Chyan, Y.; Ye, R.; Li, Y.; Singh, S. P.; Arnusch, C. J.; Tour, J. M. Laser-Induced Graphene by Multiple Lasing: Toward Electronics on Cloth, Paper, and Food. *ACS Nano* **2018**, *12*, 2176−2183.
(39) Luong, D. X.; Yang, K.; Yoon, J.; Singh, S. P.; Wang, T.; Arnusch, C. J.; Tour, J. M. Laser-Induced Graphene Composites as Multifunctional Surfaces. *ACS Nano* **2019**, *13*, 2579−2586.
(40) Ling, Y.; Pang, W.; Li, X.; Goswami, S.; Xu, Z.; Stroman, D.; Liu, Y.; Fei, Q.; Xu, Y.; Zhao, G.; Sun, B.; Xie, J.; Huang, G.; Zhang, Y.; Yan, Z. Laser-Induced Graphene for Electrothermally Controlled, Mechanically Guided, 3D Assembly and Human-Soft Actuators Interaction. *Adv. Mater.* **2020**, *32*, No. 1908475.
(41) Chen, Y.; Xie, B.; Long, J.; Kuang, Y.; Chen, X.; Hou, M.; Gao, J.; Zhou, S.; Fan, B.; He, Y.; Zhang, Y. T.; Wong, C. P.; Wang, Z.; Zhao, N. Interfacial Laser-Induced Graphene Enabling High-Performance Liquid-Solid Triboelectric Nanogenerator. *Adv. Mater.* **2021**, *33*, No. 2104290.
(42) Tao, L. Q.; Tian, H.; Liu, Y.; Ju, Z. Y.; Pang, Y.; Chen, Y. Q.; Wang, D. Y.; Tian, X. G.; Yan, J. C.; Deng, N. Q.; Yang, Y.; Ren, T. L. An Intelligent Artificial Throat with Sound-Sensing Ability Based on Laser-Induced Graphene. *Nat. Commun.* **2017**, *8*, No. 14579.
(43) Stanford, M. G.; Yang, K.; Chyan, Y.; Kittrell, C.; Tour, J. M. Laser-Induced Graphene for Flexible and Embeddable Gas Sensors. *ACS Nano* **2019**, *13*, 3474−3482.
(44) Zhang, L.; Wang, L.; Li, J.; Cui, C.; Zhou, Z.; Wen, L. Surface Engineering of Laser-Induced Graphene Enables Long-Term Monitoring of On-Body Uric Acid and pH Simultaneously. *Nano Lett.* **2022**, *22*, 5451−5458.
(45) Ye, R.; Chyan, Y.; Zhang, J.; Li, Y.; Han, X.; Kittrell, C.; Tour, J. M. Laser-Induced Graphene Formation on Wood. *Adv. Mater.* **2017**, *29*, No. 1702211.
(46) Le, T. S. D.; Lee, Y. A.; Nam, H. K.; Jang, K. Y.; Yang, D.; Kim, B.; Yim, K.; Kim, S. W.; Yoon, H.; Kim, Y. J. Green Flexible Graphene-Inorganic-Hybrid Micro-Supercapacitors Made of Fallen Leaves Enabled by Ultrafast Laser Pulses. *Adv. Funct. Mater.* **2021**, No. 2107768.
(47) Dreimol, C. H.; Guo, H.; Ritter, M.; Keplinger, T.; Ding, Y.; Gunther, R.; Poloni, E.; Burgert, I.; Panzarasa, G. Sustainable Wood Electronics by Iron-Catalyzed Laser-Induced Graphitization for Large-Scale Applications. *Nat. Commun.* **2022**, *13*, No. 3680.
(48) Bressi, A. C.; Dallinger, A.; Steksova, Y.; Greco, F. Bioderived Laser-Induced Graphene for Sensors and Supercapacitors. *ACS Appl. Mater. Interfaces* **2023**, *15*, 35788−35814.
(49) Jayan, J. S.; Jayan, S. S. Biomass-Derived Laser-Induced Graphene and Its Advances in the Electronic Applications. *Adv. Eng. Mater.* **2023**, *25*, No. 2300248.
(50) Lee, S.; Jeon, S. Laser-Induced Graphitization of Cellulose Nanofiber Substrates under Ambient Conditions. *ACS Sustainable Chem. Eng.* **2019**, *7*, 2270−2275.
(51) Le, T. S. D.; Park, S.; An, J.; Lee, P. S.; Kim, Y. J. Ultrafast Laser Pulses Enable One-Step Graphene Patterning on Woods and Leaves for Green Electronics. *Adv. Funct. Mater.* **2019**, *29*, No. 1902771.
(52) Zang, X.; Shen, C.; Chu, Y.; Li, B.; Wei, M.; Zhong, J.; Sanghadasa, M.; Lin, L. Laser-Induced Molybdenum Carbide-Graphene Composites for 3D Foldable Paper Electronics. *Adv. Mater.* **2018**, *30*, No. 1800062.
(53) Kulyk, B.; Silva, B. F. R.; Carvalho, A. F.; Silvestre, S.; Fernandes, A. J. S.; Martins, R.; Fortunato, E.; Costa, F. M. Laser-Induced Graphene from Paper for Mechanical Sensing. *ACS Appl. Mater. Interfaces* **2021**, *13*, 10210−10221.
(54) Park, H.; Kim, M.; Kim, B. G.; Kim, Y. H. Electronic Functionality Encoded Laser-Induced Graphene for Paper Electronics. *ACS Appl. Nano Mater.* **2020**, *3*, 6899−6904.
(55) Song, W.; Zhu, J.; Gan, B.; Zhao, S.; Wang, H.; Li, C.; Wang, J. Flexible, Stretchable, and Transparent Planar Microsupercapacitors Based on 3D Porous Laser-Induced Graphene. *Small* **2018**, *14*, No. 1702249.
(56) Ikram, R.; Jan, B. M.; Qadir, M. A.; Sidek, A.; Stylianakis, M. M.; Kenanakis, G. Recent Advances in Chitin and Chitosan/Graphene-Based Bio-Nanocomposites for Energetic Applications. *Polymers* **2021**, *13*, No. 3266, DOI: 10.3390/polym13193266.
(57) Roy, B. K.; Tahmid, I.; Rashid, T. U. Chitosan-Based Materials for Supercapacitor Applications: A Review. *J. Mater. Chem. A* **2021**, *9*, 17592−17642.
(58) Wang, R.; Gao, S.; Yang, Z.; Li, Y.; Chen, W.; Wu, B.; Wu, W. Engineered and Laser-Processed Chitosan Biopolymers for Sustainable and Biodegradable Triboelectric Power Generation. *Adv. Mater.* **2018**, *30*, No. 1706267.
(59) Torres, F. G.; De-la-Torre, G. E. Polysaccharide-Based Triboelectric Nanogenerators: A Review. *Carbohydr. Polym.* **2021**, *251*, No. 117055.

(60) Larrigy, C.; Burke, M.; Imbrogno, A.; Vaughan, E.; Santillo, C.; Lavorgna, M.; Sygellou, L.; Paterakis, G.; Galiotis, C.; Iacopino, D.; Quinn, A. J. Porous 3D Graphene from Sustainable Materials: Laser Graphitization of Chitosan. *Adv. Mater. Technol.* **2023**, *8*, No. 2201228.
(61) Vaughan, E.; Santillo, C.; Imbrogno, A.; Gentile, G.; Quinn, A. J.; Kaciulis, S.; Lavorgna, M.; Iacopino, D. Direct Laser Writing of Chitosan−Borax Composites: Toward Sustainable Electrochemical Sensors. *ACS Sustainable Chem. Eng.* **2023**, *11*, 13574−13583.
(62) Huang, Q.-M.; Yang, H.; Wang, S.; Liu, X.; Tan, C.; Luo, A.; Xu, S.; Zhang, G.; Ye, H. Laser-Induced Graphene Formation on Chitosan Derivatives toward Ecofriendly Electronics. *ACS Appl. Nano Mater.* **2023**, *6*, 10453−10465.
(63) Zhang, W.; Lei, Y.; Ming, F.; Jiang, Q.; Costa, P. M. F. J.; Alshareef, H. N. Lignin Laser Lithography: A Direct-Write Method for Fabricating 3D Graphene Electrodes for Microsupercapacitors. *Adv. Energy Mater.* **2018**, *8*, No. 1801840.
(64) Ferrari, A. C.; Meyer, J. C.; Scardaci, V.; Casiraghi, C.; Lazzeri, M.; Mauri, F.; Piscanec, S.; Jiang, D.; Novoselov, K. S.; Roth, S.; Geim, A. K. Raman spectrum of graphene and graphene layers. *Phys. Rev. Lett.* **2006**, *97*, No. 187401.
(65) Devi, M.; Wang, H.; Moon, S.; Sharma, S.; Strauss, V. Laser-Carbonization − A Powerful Tool for Micro-Fabrication of Patterned Electronic Carbons. *Adv. Mater.* **2023**, *35*, No. 2211054.
(66) Hong, S.; Kim, J.; Jung, S.; Lee, J.; Shin, B. S. Surface Morphological Growth Characteristics of Laser-Induced Graphene with UV Pulsed Laser and Sensor Applications. *ACS Mater. Lett.* **2023**, *5*, 1261−1270.
(67) El-Kady, M. F.; Kaner, R. B. Scalable Fabrication of High-Power Graphene Micro-Supercapacitors for Flexible and On-Chip Energy Storage. *Nat. Commun.* **2013**, *4*, No. 1475.
(68) Zhang, W.; Li, R.; Zheng, H.; Bao, J.; Tang, Y.; Zhou, K. Laser-Assisted Printing of Electrodes Using Metal-Organic Frameworks for Micro-Supercapacitors. *Adv. Funct. Mater.* **2021**, *31*, No. 2009057.

https://doi.org/10.1021/acsami.4c02139
ACS Appl. Mater. Interfaces 2024, 16, 35651−35665